scientific reports

Check for updates

OPEN

Covalently anchoring silver nanoclusters Ag_{44} on modified UiO-66-NH_2 with Bi_2S_3 nanorods and MoS_2 nanoparticles for exceptional solar wastewater treatment activity

Mostafa Farrag

For the first time, covalently anchoring size selected silver nanoclusters [Ag_{44}(MNBA)$_{30}$] on the Bi_2S_3@UiO-66-NH_2 and MoS_2@UiO-66-NH_2 heterojunctions were constructed as novel photocatalysts for photodegradation of methylene blue (MB) dye. The anchoring of Ag_{44} on MoS_2@UiO-66-NH_2 and Bi_2S_3@UiO-66-NH_2 heterojunctions extended the light absorption of UiO-66-NH_2 to the visible region and improved the transfer and separation of photogenerated charge carriers through the heterojunctions with a unique band gap structure. The UV–Vis-NIR diffuse reflectance spectroscopic analysis confirmed that the optical absorption properties of the UiO-66-NH_2 were shifted from the UV region at 379 nm to the visible region at ~ 705 nm after its doping with Bi_2S_3 nanorods and Ag_{44} nanoclusters (Bi_2S_3@UiO-66-NH-S-Ag_{44}). The prepared Bi_2S_3@UiO-66-NH-S-Ag_{44} and MoS_2@UiO-66-NH-S-Ag_{44} photocatalysts exhibited exceptional photocatalytic activity for visible light degradation of MB dye. The photocatalysts exhibited complete decolorization of the MB solution (50 ppm) within 90 and 120 min stirring under visible light irradiation, respectively. The supper photocatalytic performance and recycling efficiency of the prepared photocatalysts attributed to the covalent anchoring of the ultra-small silver clusters (Ag_{44}) on the heterojunctions surface. The X-ray photoelectron spectroscopic analysis confirmed the charge of the silver clusters is zero. The disappearance of the N–H bending vibration peak of primary amines in the FTIR analysis of Bi_2S_3@UiO-66-NH-S-Ag_{44} confirmed the covalent anchoring of the protected silver nanoclusters on the UiO-66-NH_2 surface via the condensation reaction. The Bi_2S_3@UiO-66-NH-S-Ag_{44} catalyst exhibited excellent recyclability efficiency more than five cycles without significant loss in activity, indicating their good potential for industrial applications. The texture properties, crystallinity, phase composition, particle size, and structural morphology of the prepared photocatalysts were investigated using adsorption–desorption N_2 isotherms, X-ray diffraction (XRD), HR-TEM, and FE-SEM, respectively.

Due to population growth and heavy consumption of natural resources, freshwater is becoming increasingly polluted by heavy metal ions and organic compounds[1,2]. More than 100,000 toxic and nontoxic dyes are being used for industrial purposes, a significant amount of which is released into water resources after processing[3,4]. Solar photodegradation is the best technique for the removal of dye contaminates from water[5–7].

In our previous work, a TiO_2 nanostructures were modified with two different metal chalcogenides (CuS and MoS_2), that showed high efficiency (98%) in the photodegradation of methylene blue dye under UV–Vis light irradiation[8]. Monodispersed bare silver nanoclusters with an average particle size of 1.2 nm were synthesized without protecting ligand and deposited inside the pores of a titanium dioxide modified mesoporous MCM-41

Chemistry Department, Faculty of Science, Assiut University, Assiut 71516, Egypt. email: mostafafarrag@aun.edu.eg

utilizing the novel strong electrostatic adsorption (SEA) technique[6]. The performance of the synthesized photocatalysts was tested by photocatalytic degradation of MB dye under visible light irradiation[6].

Recently, metal chalcogenides semiconductor-based photocatalysts, such as ZnS, CdS, CuS, and MoS_2 have attracted considerable attention due to their efficient photocatalytic activity toward the degradation of organic pollutants, CO_2 reduction, and water splitting, because of their low cost, narrow band gaps, relative safety, thermal stability and environmental friendly[9–12]. However, the metal chalcogenides suffer from their lower surface area, therefore constructing heterojunctions (chalcogenides/Metal–organic frameworks) photocatalysts have been considered to be an effective method to enhance the photocatalytic performance of the metal chalcogenides. A series of heterojunctions structures were prepared, such as CdS@NH_2-MIL-125(Ti), Bi_2S_3@ZiF-8(Zn), Ag_3PO_4@UiO-66, and In_2S_3@UiO-66 that exhibited highly photodegradation efficiencies for removal several organic dyes and pollutants such as rhodamine (RhB), methyl orange (MO), and phenol and oxytetracycline (OTC)[13–16]. Most importantly, as a supporting matrix, the heterojunctions can efficiently disperse semiconductor photocatalysts and provide additional channels for the timely separation of photoexcited charge carriers[17].

Metal–organic frameworks (MOFs), which are made up of metal ions linked together with organic linkers have been recognized as ideal materials due to their large surface area and tunable structures[18,19]. UiO-66 (Universitetet i Oslo) is an archetypal MOFs that is built up from $[Zr_6O_4(OH)_4(CO_2)_{12}]$ clusters linked with terephthalic acid[20,21]. The structure framework includes octahedral and tetrahedral cages in a 1:2 ratio, suitable for loading metal precursors[20,21]. UiO-66 and NH_2-UiO-66 were used in many applications due to their resistance toward a variety of organic solvents and high thermal and chemical stability[18], as well as the acidic sites of NH_2-UiO-66 that come from the Lewis acidity of the unsaturated Zr metal sites that play a significant role in the hydrolysis of $NaBH_4$[18].

Loading MOFs with metal chalcogenide semiconductors makes them more promising for absorbing light[17,22–24], whereas pure MOFs have limited spectral absorption. One of the most effective ways to improve the photocatalytic efficiency of MOFs is through heterojunction construction, which can limit charge recombination and increase light absorption in the visible light region[17,22]. Bismuth sulfide (Bi_2S_3) is a typical lamellar-structure semiconductor with a narrow band gap (~ 1.3 eV)[22], however, its application is limited due to its easy photocorrosion. As a result, combining Bi_2S_3 with MOFs to form heterojunction structures may be an option for overcoming the shortcomings of the two materials[17,22].

To further enhance the photocatalytic performance of the MOFs, metal nanoparticles have been used as doped materials not only to retard the electron–hole recombination but also to enhance visible light absorption[18,19,24–33]. Recently, protected metal nanoclusters have been used in many applications, because of their size-dependent optical and electronic properties, which differ significantly from both the single atom and bulk properties. In our previous work, we prepared several monodispersed gold[34–36], silver[6,7,37,38], platinum[5,39], and palladium[5,40,41] nanoclusters.

In this work, the NH_2-UiO-66 was chosen as a supporting matrix for many reasons such as ultrahigh porosity, high thermal and chemical stability, and high surface area[18,19]. Moreover, the negatively charged ($-NH_2$) surface of NH_2-UiO-66 allows metal ions to tightly anchor and wrap and facilitate the rapid fabrication of the Bi_2S_3@UiO-66-NH_2 and MoS_2@UiO-66-NH_2 heterojunctions. To improve the performance of the heterojunctions in the solar photodegradation of MB dye, the size selected silver nanoclusters $[Ag_{44}(MNBA)_{30}]$ is anchored onto the Bi_2S_3@UiO-66-NH_2 and MoS_2@UiO-66-NH_2 surface through a covalent interfacial reaction (condensation reaction) between the amine groups of UiO-66-NH_2 and the carboxylic groups of the protecting agent (5-mercapto-2-nitrobenzoic acid). For the first time, size selected silver nanoclusters were used as doped metal nanoparticles over the prepared heterojunctions. The field emission scanning electron microscopy (FE-SEM) results confirms the morphology of Bi_2S_3 and MoS_2 are nanorods and nanoparticles, respectively. Moreover, they are interspersed on the surface of NH_2-UiO-66 without apparent aggregation. The prepared Bi_2S_3@UiO-66-NH-S-Ag_{44} and MoS_2@UiO-66-NH-S-Ag_{44} photocatalysts exhibited exceptional photocatalytic activity and recycling for solar degradation of MB.

Experimental

Chemicals

2-Aminoterephthalic acid (H_2-BDC-NH_2) linker, *N*,*N*-dimethylformamide (DMF), zirconium chloride ($ZrCl_4$), concentrated HCl, and ethanol were purchased from Sigma–Aldrich. Bismuth nitrate pentahydrate ($Bi(NO_3)_3{\cdot}5H_2O$), sodium sulfide ($Na_2S{\cdot}9H_2O$), ethylene glycol (EG), and carbamide were purchased from Sigma–Aldrich. Ammonium molybdate tetrahydrate $(NH_4)_6Mo_7O_{24}{\cdot}4H_2O$ and thioacetamide (C_2H_5NS, 99%) were purchased from Alfa Aesar. 5,5′-Dithiobis(2-nitrobenzoic acid) (DTNBA, 99%), silver nitrate ($AgNO_3$, 99%), sodium hydroxide (NaOH), sodium borohydride ($NaBH_4$, 99.99% metals basis), and tetramethylammonium hydroxide (TMAH, 23%) were purchased from Sigma Aldrich. All chemicals were used without further purification. Methylene blue dye (MB) was used to determine the photocatalytic activity of the prepared photocatalysts.

Synthesis of UiO-66-NH_2

UiO-66-NH_2 was synthesized as reported before by the Farha group[42]. Briefly, 10 mL conc. HCl was added dropwise over suspended $ZrCl_4$ (1.25 g) in 50 mL DMF, and then the solution was sonicated for 20 min until fully dissolved. 2-Aminoterephthalic acid as linker (1.34 g) was dissolved in 100 mL DMF and added to the solution. The solution was sonicated for a further 20 min and then heated in an oven at 80 °C for 16–18 h. The resulting solid was filtered and washed with DMF (2 × 30 mL) and EtOH (2 × 30 mL). Finally, NH_2-UiO-66 was dried in an oven at 70 °C overnight. The NH_2-UiO-66 was used after activation at 150 °C for 12 h.

Synthesis of Bi_2S_3 nanorods

Bi_2S_3 nanorods were synthesized according to a previously reported method[43]. In a typical process, two solutions were prepared, solution (A) consisted of 1.82 g $Bi(NO_3)_3{\cdot}5H_2O$ that was added into 20 mL ethylene glycol (EG) under stirring for 30 min and 1.35 g Na_2S was dissolved in 20 mL DI water to form solution (B). And then solution B was added dropwise into solution A, and a black suspension appeared during the process. After that, a carbamide solution (1.92 g $CO(NH_2)_2$ in 20 mL DI H_2O) was added to the mixed solution as a pH modifier. The mixture was heated in a Teflon-lined stainless steel autoclave at 180 °C for 24 h. The product was washed with ethanol and DI water several times and dried at 60 °C to obtain Bi_2S_3 nanorods.

Synthesis of MoS_2 nanoparticles

Typically, 2.48 g of ammonium molybdate tetrahydrate $(NH_4)_6Mo_7O_{24}{\cdot}4H_2O$ (2 mmol) and 1.2 g of thioacetamide C_2H_5NS (16 mmol) was dissolved in 75 mL DI water. The solution was stirred for one hour at room temperature, ultrasonicated for 10 min, and then heated in a Teflon-lined stainless steel autoclave at 180 °C for 24 h. The product was cooled and washed with DI water several times and dried at 80 °C to obtain MoS_2 nanoparticles[44].

In-situ preparation of Bi_2S_3@UiO-66-NH_2 and MoS_2@UiO-66-NH_2 heterojunctions

The one-pot synthesis of the Bi_2S_3@NH_2-UiO-66 and MoS_2@NH_2-UiO-66 is based on the same procedure used for the preparation of NH_2-UiO-66 in section "Synthesis of UiO-66-NH_2". The Bi_2S_3 and MoS_2 in DMF were added to the NH_2-UiO-66 precursors, to immobilize the Bi_2S_3 and MoS_2 inside the NH_2-UiO-66 frameworks. After that, the precipitate was filtered and washed with DMF (2 × 30 mL) and EtOH (2 × 30 mL). Finally, the Bi_2S_3@UiO-66-NH_2 and MoS_2@UiO-66-NH_2 were dried in an oven at 70 °C overnight (Fig. 1). The loading percentage of the metal chalcogenides (Bi_2S_3 or MoS_2) was around 3%.

Synthesis and purification of $Ag_{44}(SC_6H_4O_4N)_{30}$ nanoclusters (NCs)

$Ag_{44}(SC_6H_4O_4N)_{30}$ was synthesized as reported before[45]. Briefly, 9.91 mg of 5,5′-dithiobis(2-nitrobenzoic acid) (DTNBA) was stirred in 20 mL NaOH aqueous solution (1 M). The disulfide bond was cleaved which was indicated by the formation of a dark yellow solution from 5-mercapto-2-nitrobenzoic acid (MNBA). 8.5 mg of $AgNO_3$ (50 mmol) was dissolved in 5 mL DI water and added to the MNBA solution. The color was changed from dark yellow to greenish yellow indicating the formation of an Ag–S complex. A fresh $NaBH_4$ solution (1 mg in 2 mL DI water) was then used to reduce the complex. The solution turned dark brown immediately and gradually changed to dark red under vigorous stirring for 4 h, indicating the formation of $Ag_{44}(SR)_{30}$ NCs. The clusters were purified by repeated precipitation with 50% methanol followed by repeated centrifugation at 9000 rpm for 10 min and decantation of the supernatant until it became colorless.

Covalently anchoring of Ag_{44} on Bi_2S_3@UiO-66-NH_2 and MoS_2@UiO-66-NH_2

100 mg Bi_2S_3@UiO-66-NH_2 or MoS_2@UiO-66-NH_2 was dispersed in 40 mL DI water and sonicated for 30 min. 5 mg of $Ag_{44}(SC_6H_4O_4N)_{30}$ nanoclusters in methanol was added over the suspension and sonicated for 30 min. The final solution was heated at 80 °C, for 2 h and then stirred overnight at room temperature. The products

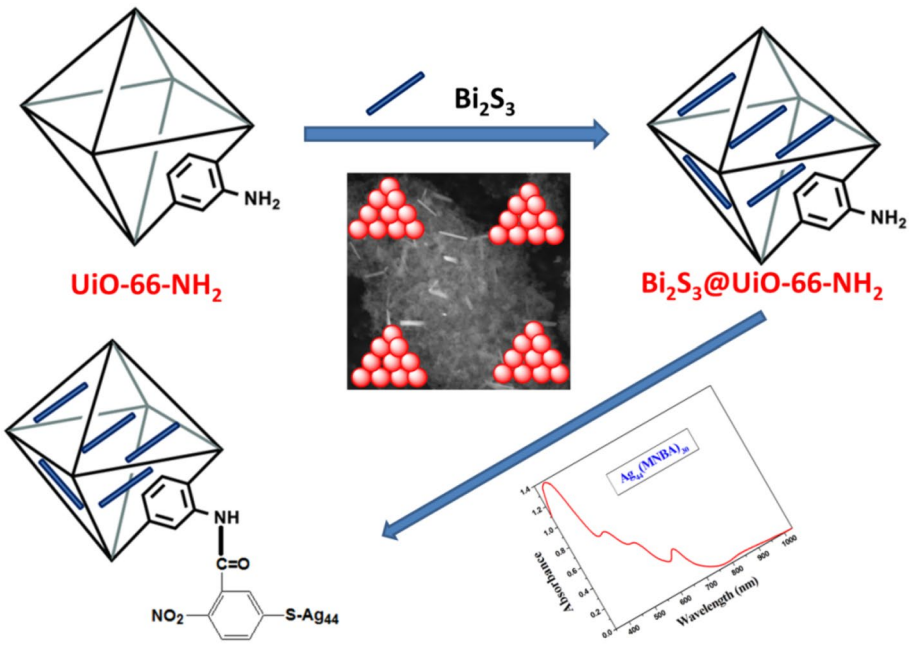

Figure 1. Scheme of the preparation of Bi_2S_3@UiO-66-NH-S-Ag_{44} photocatalysts.

donated as Bi_2S_3@UiO-66-NH-S-Ag_{44} (Fig. 1) or MoS_2@UiO-66-NH-S-Ag_{44} were collected by filtration and then dried in an oven overnight[17].

Photocatalytic studies of the prepared photocatalysts

The photocatalytic degradation of methylene blue (MB) solution using visible light was carried out to evaluate the photocatalytic activity of the prepared photocatalysts. A 450 W medium-pressure mercury lamp with a < 420 nm UV cut-off filter was used as a visible light source for the photocatalytic experiments, the lamp was fixed 10 cm away from the reaction system, as used in our previous work[5,6, 46–48]. 30 mg of the prepared photocatalysts were suspended in 50 mL of highly concentrated aqueous solution MB (50 ppm) under magnetic stirring. To establish an adsorption–desorption equilibrium, the reaction system was first kept in the dark for 60 min and then exposed to visible light for two hours. 5 mL aliquots from each sample were taken at the desired time intervals, followed by centrifugation and filtration to remove the photocatalyst. The decolorization of the MB solution was evaluated by measuring the change in its characteristic optical absorbance using an Evolution 300 UV–Vis spectrophotometer[5,6]. To check the advantages of the prepared photocatalysts and their applicability to reuse[5,6], the photodegradation reaction of the MB solution was achieved with Bi_2S_3@UiO-66-NH-S-Ag_{44} photocatalyst. Then the photocatalyst was collected at the end of the reaction and reused for a second cycle and the process repeated so on till five cycles keeping all other parameters constant.

Results and discussion

Atomically precise monodispersed thiol-protected silver nanoclusters [$Ag_{44}(MNBA)_{30}$] were synthesized using 5-mercapto-2-nitrobenzoic acid as a protecting ligand (Fig. S1). The used method produced monodisperse and stable silver nanoclusters in aqueous solution for at least 9 months at room temperature under ambient conditions. Electrospray ionization mass spectrometry (ESI–MS) was used to determine the composition, size, and monodispersity of the clusters[45]. The silver nanoclusters [$Ag_{44}(MNBA)_{30}$] showed at least five characteristic absorption peaks in the visible-NIR region with absorption maxima at 400, 480, 550, 650, and 850 nm (Fig. S2).

Characterization of the prepared photocatalysts

The crystallinity phase composition, texture properties, structure morphology, and particle size of the prepared photocatalysts were characterized by X-ray diffraction (XRD), adsorption–desorption N_2 isotherms, FE-SEM, and HR-TEM, respectively. The chemical structure and the stoichiometry and charge of the prepared photocatalysts were investigated by FT-IR and X-ray photoelectron spectroscopy (XPS), respectively. The UV–Vis diffuse reflectance spectroscopic analysis was used to investigate the optical absorption properties and the band-gap of the prepared photocatalysts[49].

The XRD patterns of the prepared photocatalysts were presented in Fig. 2I, which confirms the successful fabrication of Bi_2S_3 nanorods, MoS_2 nanoparticles, NH_2-UiO-66, MoS_2@UiO-66-NH-S-Ag_{44}, and Bi_2S_3@UiO-66-NH-S-Ag_{44} photocatalysts. The Bi_2S_3 nanorods exhibited XRD diffraction peaks at 2θ = 15.8°, 17.6°, 22.6°, 23.8°, 25.2°, 27.39°, 28.6°, 32°, 33.18°, 33.98°, 35.77°, 36.77°, 39.17°, 40.17°, 45.76° and 46.56°, corresponding to the (020), (120), (220), (101), (130), (021), (211), (221), (301), (311), (240), (231), (041), (141), (002) and (431) planes, respectively (Fig. 2Ia), which are matched well with the previous reported work[43], and the JCPDS card no. 17-0320. The MoS_2 shows weak intensity diffraction peaks in comparison to the diffraction peaks of Bi_2S_3, indicating the poor crystallinity and lower particle size of the prepared MoS_2 nanoparticles (Fig. 2Ib), the XRD diffraction peaks of the MoS_2 at 2θ = 12.6°, 16.35°, 19°, 25.4° and 29.7° are corresponding to the (002), (004), (100), (102) and (103) planes and the JCPDS card no. 65–0160[50], respectively. The characteristic diffraction peaks at 2θ = 7.3°, 8.5°, and 25.7°[18,19], corresponding to the (111), (200), and (531) planes of NH_2-UiO-66, respectively

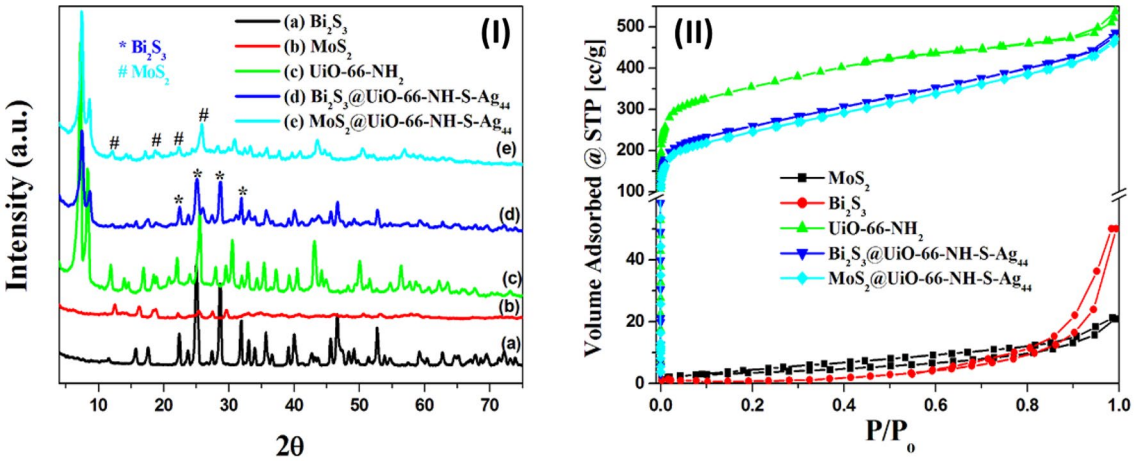

Figure 2. (**I**) X-ray diffractograms of the prepared photocatalysts, (**a**) Bi_2S_3, (**b**) MoS_2, (**c**) UiO-66-NH_2, (**d**) Bi_2S_3@UiO-66-NH-S-Ag_{44}, and (**e**) MoS_2@UiO-66-NH-S-Ag_{44}. (**II**) The nitrogen adsorption–desorption isotherms of Bi_2S_3, MoS_2, UiO-66-NH_2, Bi_2S_3@UiO-66-NH-S-Ag_{44}, and (**e**) MoS_2@UiO-66-NH-S-Ag_{44}.

(Fig. 2Ic). As shown in the Fig. 2Id the two components of the Bi_2S_3@UiO-66-NH-S-Ag_{44} photocatalyst were observed, which suggests the successful combination of the Bi_2S_3 nanorods and NH_2-UiO-66. The diffraction peaks at 7.5° and 8.5° are identified for the NH_2-UiO-66 and the diffraction peaks at 2θ = 22.6°, 25.2°, 28.6° and 32° (labeled with a '*' mark) are corresponding to Bi_2S_3 (Fig. 2Id). The same case appeared in the MoS_2@UiO-66-NH-S-Ag_{44}, the characteristic diffraction peaks of the MoS_2 are labeled with a '#' mark (Fig. 2Ie). There is no characteristic XRD peak for silver nanoclusters (Ag_{44}) in Fig. 2Id,e, due to its high dispersion inside the MOF's skeleton structure and the lower loading percentage[18].

The textural properties of the prepared photocatalysts were investigated using the N_2 adsorption–desorption isotherms at 77 K, as shown in Fig. 2II. The specific surface area (S_{BET}) and the pore volume distribution of the prepared photocatalysts were determined using the Brunauer–Emmett–Teller (BET) equation and the Barrett- Joyner-Halenda (BJH) method[6,18], respectively. The S_{BET} of the pure NH_2-UiO-66 is 1106 m^2/g with a total pore volume of 0.40 cm^3/g[18]. The specific surface area and pore volume of the NH_2-UiO-66 were decreased after loading with Bi_2S_3 or MoS_2 and Ag_{44} as shown in Table 1. All of them showed isotherms belonging to type I with H4 hysteresis loops, corresponding to the IUPAC classification of the hysteresis loops, these materials have mesoporous pores[51]. However, the synthesized metal chalcogenides (Bi_2S_3 and MoS_2) exhibited lower specific surface areas (Table 1). The surface areas of the prepared photocatalysts were measured by another method (T-method, S_t). The values of S_t are equal S_{BET}, which confirms the correct choice of the standard t-curves (Table 1).

FTIR analysis was carried out to verify the formation of linkages between the NH_2-UiO-66 and the protected silver nanoclusters [Ag_{44}(MNBA)$_{30}$] via a condensation reaction. Figure 3Ia shows the FTIR spectrum of the pristine NH_2-UiO-66, where the absorption peaks at 3440 cm^{-1} and 1577 cm^{-1} are assigned to the amino N–H and carbonyl C=O groups, respectively[17]. The C–N stretching vibration modes show two absorption bands at around 1360 cm^{-1} and 1259 cm^{-1}. The absorption bands between 768 cm^{-1} and 572 cm^{-1} are assigned to the Zr–O modes. The C = C skeletal vibration of the benzene ring shows an absorption peak at 1566 cm^{-1} in NH_2-UiO-66[17]. No significant differences were observed between the FTIR spectra of MoS_2@UiO-66-NH-S-Ag_{44} (Fig. 3Ib) and Bi_2S_3@UiO-66-NH-S-Ag_{44} (Fig. 3Ic) in comparison to NH_2-UiO-66, confirming the existence of NH_2-UiO-66 in the photocatalysts, instead of the absences of the N–H bending vibration peak of primary amines that observed in the region 1650–1580 cm^{-1} as shown in Fig. 3II, due to the covalent anchoring of the protected silver clusters throw the condensation reaction between the NH_2 group of NH_2-UiO-66 and the carboxylic group of the 5-mercapto-2-nitrobenzoic acid ligand.

The morphological characteristics of the Bi_2S_3@UiO-66-NH-S-Ag_{44} and MoS_2@UiO-66-NH-S-Ag_{44} and the particle size of the loaded silver nanoclusters were identified by High resolution-transmission electron

Catalysts	S_{BET} ($m^2\ g^{-1}$)	S_t ($m^2\ g^{-1}$)	Pore volume (cm^3/g) × 10^{-3}
NH_2-UiO-66	1106	1106	400
Bi_2S_3@UiO-66-NH-S-Ag_{44}	805	804	335
MoS_2@UiO-66-NH-S-Ag_{44}	769	770	312
Bi_2S_3	22	22	55
MoS_2	8	8	20

Table 1. Surface area data for the prepared photocatalysts.

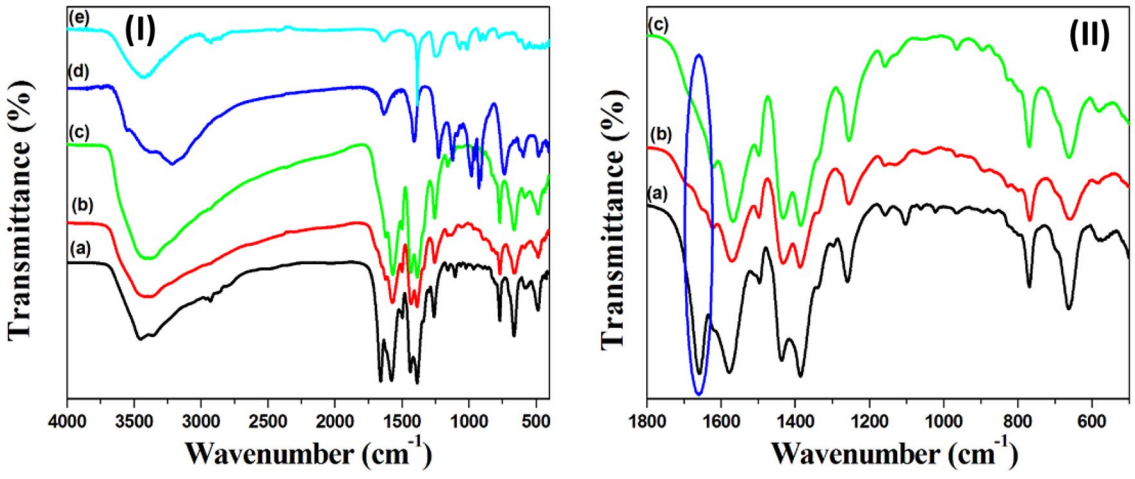

Figure 3. (**I**) FT-IR spectra of (**a**) UiO-66-NH_2, (**b**) MoS_2@UiO-66-NH-S-Ag_{44}, (**c**) Bi_2S_3@UiO-66-NH-S-Ag_{44} (**d**) MoS_2 and (**e**) Bi_2S_3. (**II**) FT-IR spectra of (**a**) UiO-66-NH_2, (**b**) MoS_2@UiO-66-NH-S-Ag_{44}, (**c**) Bi_2S_3@UiO-66-NH-S-Ag_{44} from 500 to 1800 cm^{-1}.

microscopy (HR-TEM) (Fig. 4I,II), respectively. The octahedral morphology with very smooth crystals of the pristine NH_2-UiO-66, as reported before in our previous work[18,19] does not appear in the case of Bi_2S_3@UiO-66-NH-S-Ag_{44} (Fig. 4I) and MoS_2@UiO-66-NH-S-Ag_{44} (Fig. 4II), and the surface becomes rough, due to the complete encapsulation of the Bi_2S_3 and MoS_2 by NH_2-UiO-66. There are homogenous black dots inside the blue circle of the TEM images of Bi_2S_3@UiO-66-NH-S-Ag_{44} and MoS_2@UiO-66-NH-S-Ag_{44}, which refer to the silver nanoclusters (Ag_{44}) with an average particle size of ~ 1.5 nm as shown in Fig. S1, Fig. 4I,II. The inset images in Fig. 4I,II refer to the crystallinity of the prepared Bi_2S_3@UiO-66-NH-S-Ag_{44} and MoS_2@UiO-66-NH-S-Ag_{44} photocatalysts. The high magnification FE-SEM images of Bi_2S_3@UiO-66-NH-S-Ag_{44} (Fig. 4III) and MoS_2@UiO-66-NH-S-Ag_{44} (Fig. 4IV) indicate that the Bi_2S_3 and MoS_2 appear as nanorods and nanoparticles over the surface and inside the cavities of the NH_2-UiO-66 without apparent aggregation.

To estimate the valence state of the covalently anchoring silver nanoclusters and the elemental content of the prepared Bi_2S_3@UiO-66-NH-S-Ag_{44} (Fig. 5) and MoS_2@UiO-66-NH-S-Ag_{44} (Fig. 6) photocatalysts, the X-ray photoelectron spectroscopy (XPS) measurements were conducted. Figure 5I displays a typical survey spectrum of the Bi_2S_3@UiO-66-NH-S-Ag_{44} and confirms the existence of Bi 4f, 4d and 5d, Zr 3d, S 2s and 2p, C 1s, O 1s, N 1s, and Ag 3d. The Zr, C, and O elements show the strongest peaks in the survey spectrum, with a small peak of N indicating the crystal lattice of NH_2-UiO-66. To indicate the presence of the Bi_2S_3 in the prepared photocatalyst the high-resolution XPS spectra of Bi and S are analyzed separately, as shown in Fig. 5II,III, respectively. The binding energy peaks at 158.5 eV and 163.8 eV were ascribed for Bi $4f_{7/2}$ and Bi $4f_{5/2}$ (Fig. 5II) and the peaks at 161.9 eV and 163.12 eV observed for S $2p_{3/2}$ and S $2p_{1/2}$ transitions (Fig. 5III), respectively[1,17]. The chemical states of Bi and S were Bi^{3+} and S^{2-} in the loaded Bi_2S_3, which are following the previous literature[1,17]. The XPS analysis was used to determine the charge of the covalently anchoring Ag_{44} nanoclusters in the Bi_2S_3@UiO-66-NH_2 photocatalyst. The XPS spectrum of Ag 3d shows two peaks at binding energy around 368 eV and 374 eV, corresponding to Ag $3d_{5/2}$ and Ag $3d_{3/2}$, respectively (Fig. 5IV). This is a characteristic peaks for the metallic silver (Ag^0)[6]. This confirms the covalently anchoring silver nanoclusters (Ag_{44}) have zero charge[45].

The MoS_2@UiO-66-NH-S-Ag_{44} photocatalyst shows the same XPS survey spectrum of the Bi_2S_3@UiO-66-NH-S-Ag_{44} with the same elements, instead of replacing the Bi with the Mo element (Fig. 6I). The high-resolution XPS spectrum of the Mo element exhibited two binding energy peaks at 229.2 eV and 232.4 eV that can be assigned to the Mo $3d_{5/2}$ and Mo $3d_{3/2}$[52], respectively (Fig. 6II). The sulfur element in the MoS_2@UiO-66-NH-S-Ag_{44} exhibited

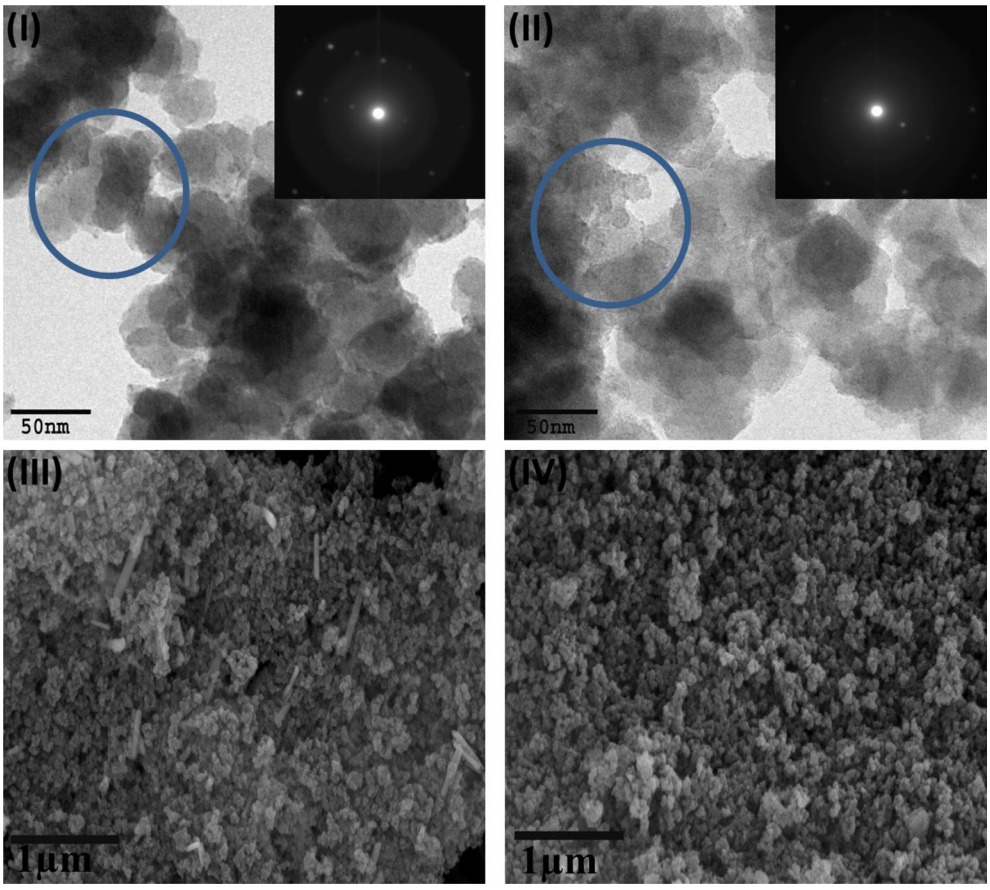

Figure 4. High resolution-transmission electron microscopy (HR-TEM) images of the Bi_2S_3@UiO-66-NH-S-Ag_{44} (**I**) and MoS_2@UiO-66-NH-S-Ag_{44} (**II**). FE-SEM images of Bi_2S_3@UiO-66-NH-S-Ag_{44} (**III**) and MoS_2@UiO-66-NH-S-Ag_{44} (**IV**).

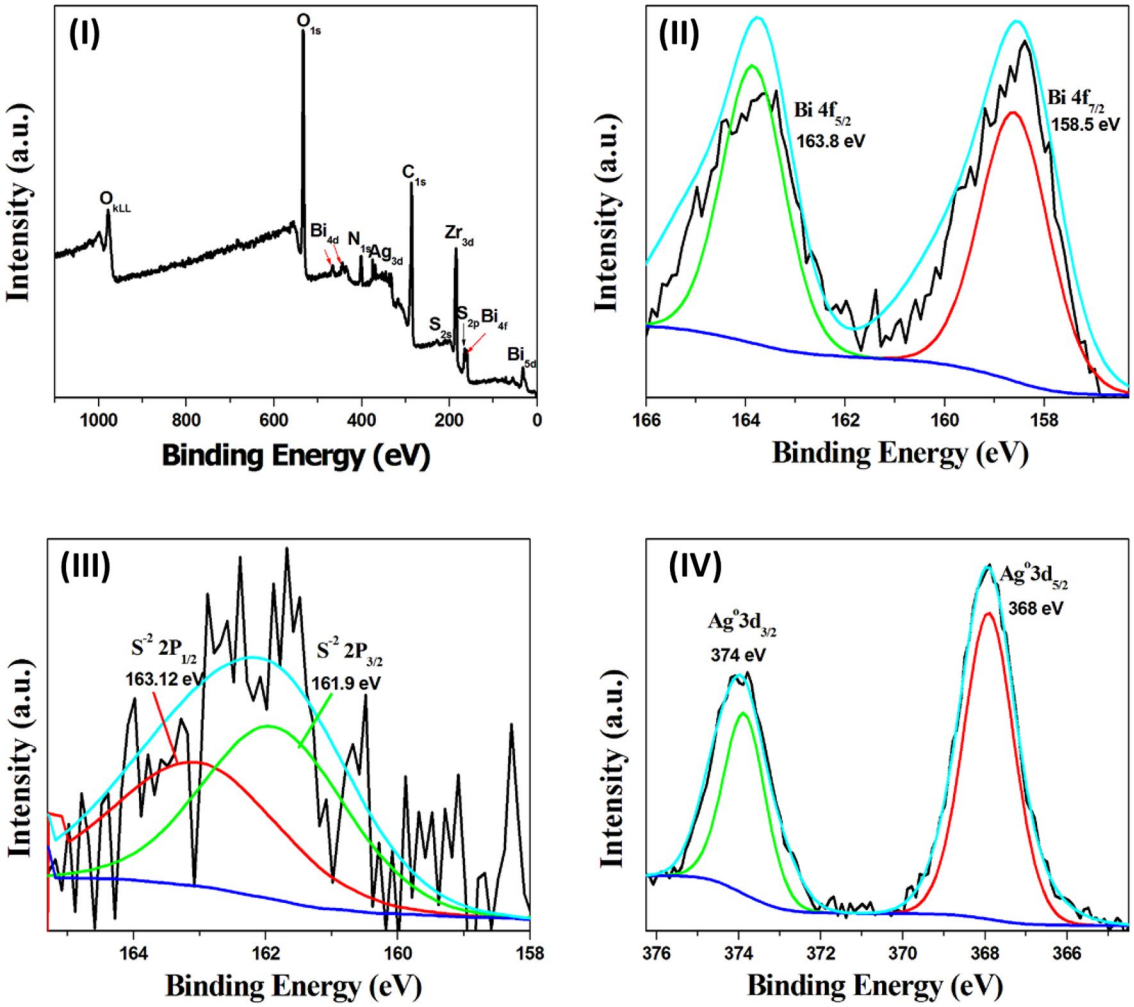

Figure 5. High-resolution X-ray photoelectron spectroscopy (HR-XPS) spectra of the Bi_2S_3@UiO-66-NH-S-Ag_{44} photocatalyst, (**I**) survey spectrum, (**II**) the XPS spectrum of Bi 4f., (**III**) the XPS spectrum of S 2p and (**IV**) the XPS spectrum of Ag 3d.

the same two binding energy peaks at 161.9 eV and 163.1 eV (Fig. 6III). Figure 6IV exhibited two binding energy peaks at 368.1 eV and 374 eV that are corresponding to metallic silver (Ag^0).

To measure the optical response of the pure UiO-66-NH_2, Bi_2S_3, and MoS_2 and the prepared photocatalysts (Bi_2S_3@UiO-66-NH-S-Ag_{44} and MoS_2@UiO-66-NH-S-Ag_{44}) the diffuse reflectance spectra (DRS) of the powder samples were recorded. The Kubelka–Munk (K-M) equation was used to correlate the absorbance of the samples with the diffuse reflectance[23]. Figure 7I exhibited the plot of the K-M function of the prepared photocatalysts depicting the K-M plots and Fig. 7II shows the corresponding $(F(R)h\nu)^{1/2}$ vs. hν plot for the calculation of effective indirect band gap of the prepared photocatalysts.

Figure 7Ia exhibited the UV–Vis-NIR diffuse reflectance spectrum of the pure UiO-66-NH_2 with two distinct peaks. The first peak centered at ~ 230 nm originated from the electron transition from the organic linker to the Zr–O cluster. The second strong peak centered at ~ 360 nm is attributed to the substitution of $-NH_2$ in the organic linker[24]. The pure Bi_2S_3 shows a broad absorption peak that extended from UV to the near-infrared (NIR) region (300–1000 nm) and is centered at 705 nm (Fig. 7Ie), also the absorption range of the pure MoS_2 covers the whole UV and visible light region (Fig. 7Id), which indicates the prepared metal chalcogenides have an excellent optical response. Compared to NH_2-UiO-66, Bi_2S_3@UiO-66-NH-S-Ag_{44} (Fig. 7Ic) and MoS_2@UiO-66-NH-S-Ag_{44} (Fig. 7Ib) exhibit an extended absorption in the whole visible light region and near-infrared (NIR) region, due to the special electronic distribution for the covalently anchoring silver nanoclusters (Ag_{44}) and the doped optically active metal chalcogenides. The band gap values were calculated by the Kubelka–Munk from the extrapolation of the linear portion at $(F(R)h\nu)^{1/2} = 0$ providing the effective indirect band gap of the prepared photocatalysts (Fig. 7II). The band gaps of the pure NH_2-UiO-66 and Bi_2S_3 were calculated to be 2.87 eV and 1.28 eV, respectively (Fig. 7II).

Photocatalytic activity of the prepared photocatalysts under visible light irradiation

Methylene blue (MB) dye was chosen as a pollutant model to investigate the adsorption and photocatalytic activities of the prepared photocatalysts. A UV–Vis spectrophotometer (Evolution 300) was used to evaluate

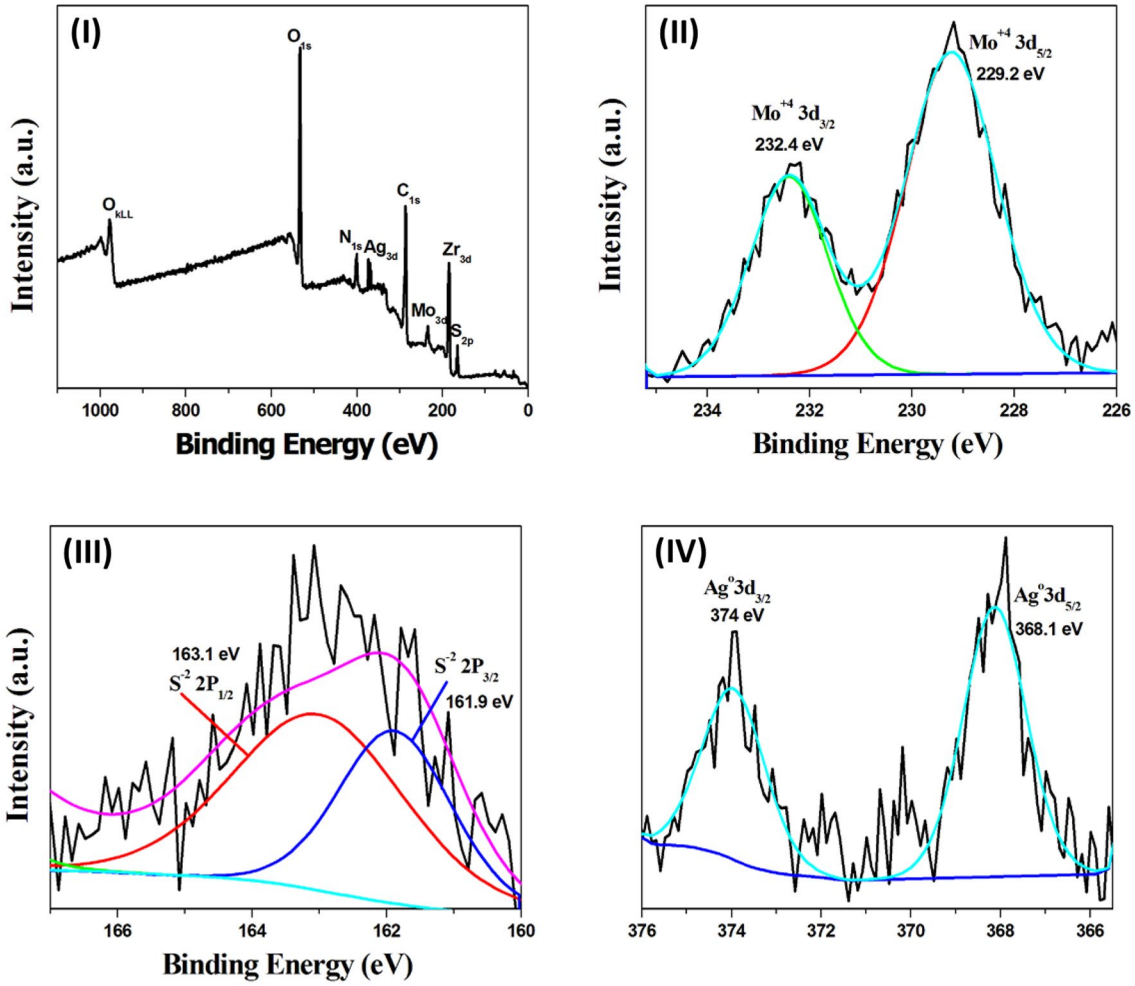

Figure 6. High-resolution X-ray photoelectron spectroscopy (HR-XPS) spectra of the MoS_2@UiO-66-NH-S-Ag_{44} photocatalyst, (**I**) survey spectrum, (**II**) the XPS spectrum of Mo 3d, (**III**) the XPS spectrum of S 2p and (**IV**) the XPS spectrum of Ag 3d.

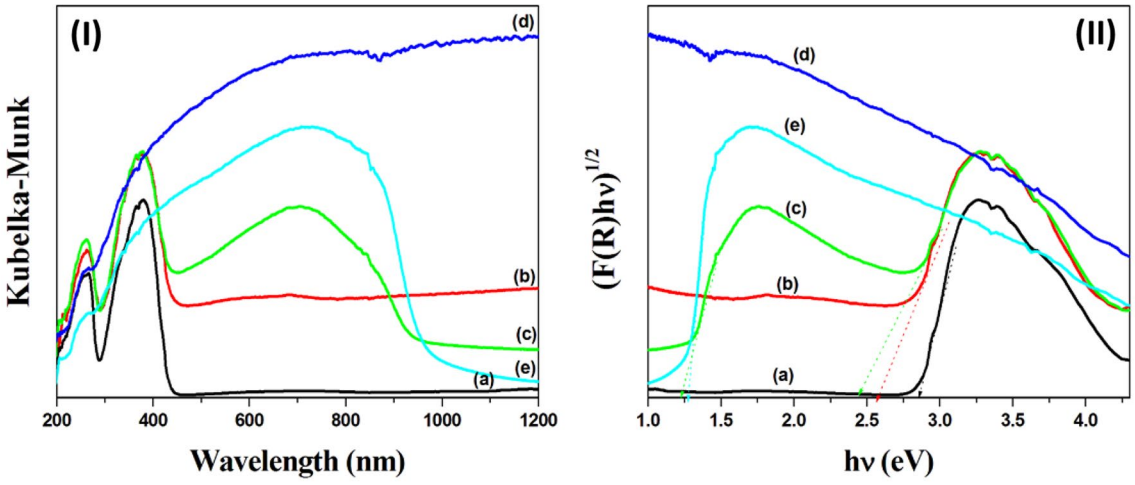

Figure 7. The UV–Vis-NIR diffuses reflectance spectra (**I**) and the plots of transformed K-M function (**II**) for the prepared photocatalysts (**a**) UiO-66-NH_2, (**b**) MoS_2@UiO-66-NH-S-Ag_{44}, (**c**) Bi_2S_3@UiO-66-NH-S-Ag_{44} (**d**) MoS_2 and (**e**) Bi_2S_3.

the photodegradation reaction. It is well known that the MB molecule is stable under visible light irradiation without photocatalyst[17].

As shown in Fig. 8a, the NH_2-UiO-66 sample shows the highest adsorption properties compared to the prepared MoS_2 and Bi_2S_3 (Fig. 8b,c), respectively, due to its large surface area of 1106 m^2/g and ordered nanosized channels, but the photodegradation activity of the NH_2-UiO-66 is low due to its absorption properties is limited in the UV region, as confirmed by UV–Vis diffuse reflectance analysis (Fig. 7Ia).

The photocatalytic activity of the Bi_2S_3@UiO-66-NH_2 and MoS_2@UiO-66-NH_2 heterojunctions is 56% and 49% in comparison to the pure UiO-66-NH_2 (18%), indicating the synergistic effect between UiO-66-NH_2 and Bi_2S_3 and MoS_2 (Fig. 8e,d), respectively. Modification of UiO-66-NH_2 with metal chalcogenides semiconductors (Bi_2S_3 and MoS_2) plays an important role in the photocatalytic degradation of MB dye (Fig. 8e,d). Due to the Bi_2S_3 and MoS_2 delay the recombination of the electron–hole pairs, enhance the conduction of charge carriers of UiO-66-NH_2 and redshift the optical absorption of UiO-66-NH_2 from the UV region (379 nm) to visible region at ~ 705 nm, as confirmed by the UV–Vis diffuse reflectance spectroscopic analysis (Fig. 7).

The MoS_2@UiO-66-NH_2 and Bi_2S_3@UiO-66-NH_2 heterojunctions were covalently anchored with the size selected silver nanoclusters (Ag_{44}) that show extremely photocatalytic activity in the photodegradation of the MB solution (Fig. 8f,g), respectively. The 50 ppm MB solution was destroyed over the MoS_2@UiO-66-NH-S-Ag_{44} and Bi_2S_3@UiO-66-NH-S-Ag_{44} photocatalysts within 120 and 90 min stirring at room temperature under visible light illumination, respectively.

The extremely photocatalytic activity of the prepared photocatalysts was attributed to their amazing optical absorption properties. The Bi_2S_3@UiO-66-NH_2 heterojunction absorbs in visible region at ~ 705 nm. The covalently anchoring zero charge silver clusters (Ag_{44}) enhanced this absorption as shown in Fig. 7, due to the silver clusters have special optical properties, where it have five characteristic absorption peaks in the visible-NIR region with absorption maxima at 400, 480, 550, 650, and 850 nm, as shown in Fig. S2.

The elemental trapping experiments have been performed to investigate the contribution of active species during the photocatalytic degradation of MB. P-benzoquinone (BQ), ethylene diamine tetraacetic acid disodium (EDTA-2Na) and isopropanol (IPA) were used as scavengers to quench the superoxide radical $O_2^{\cdot-}$, photogenerated holes h^+ and free radical hydroxide ·OH, respectively. As shown in Fig. 9I, the photodegradation of MB over Bi_2S_3@UiO-66-NH-S-Ag_{44} photocatalyst without any scavenger reached 100% under visible irradiation for 90 min. The addition of IPA decreased the activity to 63%, while the degradation efficiency quenched to 92% and 81% when using p-BQ and EDTA-2Na, respectively. These results indicate that ·OH radical is the major active species for the MB degradation reaction. However, h^+ and $O_2^{\cdot-}$ have a minor effect on the photocatalytic process[8].

The covalently anchoring silver nanoclusters on the MoS_2@UiO-66-NH_2 and Bi_2S_3@UiO-66-NH_2 heterojunctions are not only enhancing the photocatalytic activity but also the recyclability properties. Where, Bi_2S_3@UiO-66-NH-S-Ag_{44} photocatalyst shows a very good activity for at least five catalytic runs without any loss in the photocatalytic degradation of MB (Fig. 9II). This means, these photocatalysts possess high stability and may be reusable for at least 5 runs, showing a good potential for industrial applications. This recyclability efficiency confirms a very low silver clusters leaching from the MoS_2@UiO-66-NH_2 and Bi_2S_3@UiO-66-NH_2 surface. That was confirmed by measuring the XPS analysis for the catalyst before and after each recycling run, where the percentage of silver clusters remains nearly constant.

In the light of the previous discussion, the possible mechanism for MB photodegradation over the Bi_2S_3@UiO-66-NH-S-Ag_{44} photocatalyst is shown in Fig. S3. Under visible light illumination, UiO-66-NH_2 modified by Bi_2S_3 and Ag_{44} was excited, leading to the generation of charge carriers. The photoexcited electrons on the conduction band (CB) of Bi_2S_3 could transfer directly to the CB of the UiO-66-NH_2. Meanwhile, the valence band (VB) of UiO-66-NH_2 (2.27)[53] is more positive than Bi_2S_3 (1.48)[54], thus the photoexcited holes migrate in the reverse direction of electrons (Fig. S3).

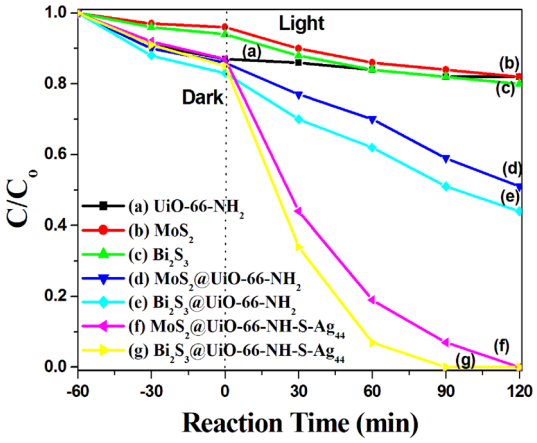

Figure 8. The photocatalytic decomposition of 50 ml (50 ppm) methylene blue (MB) dye over 30 mg of the prepared photocatalysts.

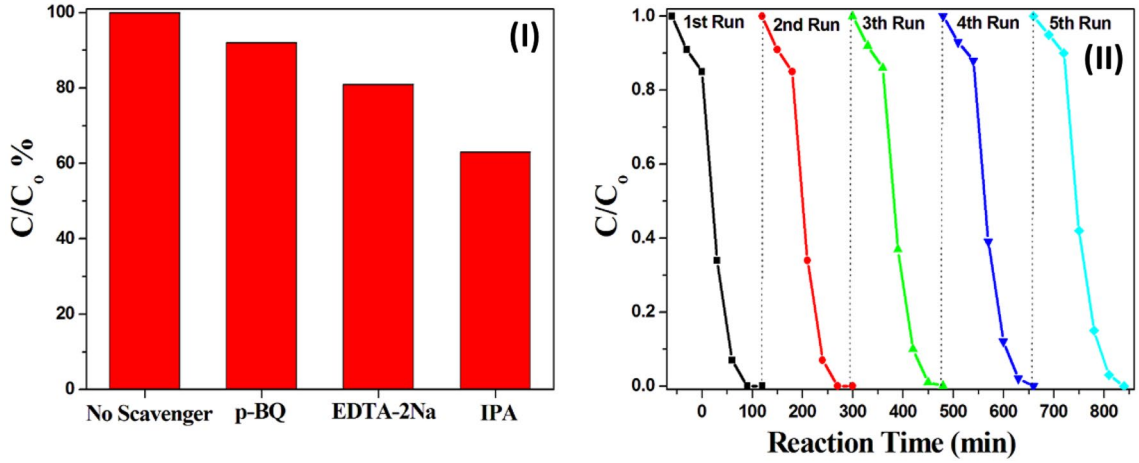

Figure 9. (**I**) Trapping experiments of active species over Bi_2S_3@UiO-66-NH-S-Ag_{44}. (**II**) Recyclability effect of the Bi_2S_3@UiO-66-NH-S-Ag_{44} photocatalyst was studied for visible light degradation of MB solution.

A comparison among different metal chalcogenides and Metal–organic frameworks photocatalysts that were reported as photocatalysts for the photodegradation of organic dyes is tabulated in Table 2.

Conclusion

In summary, we have successfully prepared Bi_2S_3@UiO-66-NH-S-Ag_{44} and MoS_2@UiO-66-NH-S-Ag_{44} photocatalysts through a condensation reaction for solar degradation of MB dye. Where the size selected silver nanoclusters [$Ag_{44}(MNBA)_{30}$] are anchored onto the Bi_2S_3@UiO-66-NH_2 and MoS_2@UiO-66-NH_2 surface through a covalent interfacial reaction between the amine groups of UiO-66-NH_2 and the carboxylic groups of the 5-mercapto-2-nitrobenzoic acid ligand. The covalently anchoring silver nanoclusters on the UiO-66-NH_2 surface were confirmed by FTIR analysis, where the N–H bending vibration peak at 1650–1580 cm^{-1} was disappeared in the MoS_2@UiO-66-NH-S-Ag_{44} and Bi_2S_3@UiO-66-NH-S-Ag_{44} FTIR spectra. The prepared Bi_2S_3@UiO-66-NH-S-Ag_{44} and MoS_2@UiO-66-NH-S-Ag_{44} photocatalysts exhibited amazing photocatalytic activity and recyclability in the photodegradation of MB dye. The super photocatalytic performance of the prepared photocatalysts was attributed to the interfacial compactness of the silver nanoclusters in the heterojunction structure, which does not suffer from any leaching. Moreover, the doping of UiO-66-NH_2 with Bi_2S_3 and silver clusters shift the optical absorption properties of UiO-66-NH_2 from the UV region (379 nm) to the visible region at ~ 705 nm, as confirmed by the UV–Vis-NIR diffuse reflectance spectroscopic analysis. The prepared photocatalysts have high crystallinity properties as confirmed by XRD analysis and their textural properties were investigated with nitrogen adsorption–desorption isotherms at − 196 °C.

Photocatalysts	Pollutant content (mg/L)	Light Source	% of Degradation	Refs
Ca/TiO_2/NH_2-MIL-125	40	300 W Xe lamp	86.2	[55]
CoS_x/NH_2-MIL-125	20	300 W Xe lamp	95.4	[56]
BiOBr/NH_2-MIL-125	20	500 W Xe lamp	93	[57]
MoS_2/TiO_2	5	400 W Xe Lamp	99.3	[58]
CuxS/TiO_2	10	Visible light	95	[59]
CdS/TiO_2	12	160 W Hg lamp	93.8	[60]
PbS/GR/TiO_2	1×10^{-4} M	Visible light	41	[61]
MoS_2@UiO-66-NH-S-Ag_{44}	50	450 W Hg lamp Visible light	99.8	This work
Bi_2S_3@UiO-66-NH-S-Ag_{44}	50	450 W Hg lamp Visible light	100	This work

Table 2. Comparison table on photodegradation of MB dye.

Data availability

All data generated or analyzed during this study are included in this published article (and its supplementary information files).

Received: 17 July 2023; Accepted: 12 October 2023
Published online: 17 October 2023

References

1. Wang, Y. *et al.* Fabrication of Bi_2S_3/MOFs composites without noble metals for enhanced photoreduction of Cr (VI). *Sep. Purif. Technol.* **241**, 116703 (2020).
2. Liu, Y. *et al.* Synthesis of nano SnO_2-coupled mesoporous molecular sieve titanium phosphate as a recyclable photocatalyst for efficient decomposition of 2, 4-dichlorophenol. *Nano Res.* **11**, 1612–1624 (2018).
3. Robinson, T. *et al.* Remediation of dyes in textile effluent: A critical review on current treatment technologies with a proposed alternative. *Bioresour. Technol.* **77**(3), 247–255 (2001).
4. Padhi, B. Pollution due to synthetic dyes toxicity & carcinogenicity studies and remediation. *Int. J. Environ. Sci.* **3**(3), 940–955 (2012).
5. Farrag, M. Preparation, characterization and photocatalytic activity of size selected platinum nanoclusters. *J. Photochem. Photobiol. A* **318**, 42–50 (2016).
6. Farrag, M. Electrostatic adsorption of ultra-small silver nanoclusters on titanium dioxide modified mesoporous MCM-41as a high-performance photocatalyst for wastewater treatment. *J. Photochem. Photobiol. A* **422**, 113551 (2022).
7. Farrag, M. & Mohamed, R. A. Ecotoxicity of ~1 nm silver and palladium nanoclusters protected by l-glutathione on the microbial growth under light and dark conditions. *J. Photochem. Photobiol. A* **330**, 117–125 (2016).
8. El-Gendy, R. A. *et al.* Metal chalcogenides (CuS or MoS_2)-modified TiO_2 as highly efficient bifunctional photocatalyst nanocomposites for green H2 generation and dye degradation. *Sci. Rep.* **13**(1), 7994 (2023).
9. Tan, Y. *et al.* A novel UiO-66-NH2/Bi2WO6 composite with enhanced pollutant photodegradation through interface charge transfer. *Colloids Surf. A* **622**, 126699 (2021).
10. Jiang, Y. *et al.* Construction of immobilized CuS/TiO2 nanobelts heterojunction photocatalyst for photocatalytic degradation of enrofloxacin: Synthesis, characterization, influencing factors and mechanism insight. *J. Chem. Technol. Biotechnol.* **94**(7), 2219–2228 (2019).
11. Du, J. *et al.* Highly efficient hydrogen evolution catalysis based on MoS_2/CdS/TiO_2 porous composites. *Int. J. Hydrog. Energy* **43**(19), 9307–9315 (2018).
12. Hao, X. *et al.* Zn-vacancy mediated electron-hole separation in ZnS/g-C_3N_4 heterojunction for efficient visible-light photocatalytic hydrogen production. *Appl. Catal. B* **229**, 41–51 (2018).
13. Zhang, N. *et al.* Heterostructural Ag_3PO_4/UiO-66 composite for highly efficient visible-light photocatalysts with long-term stability. *J. Photochem. Photobiol., A* **376**, 305–315 (2019).
14. Wang, H. *et al.* Controllable self-assembly of CdS@ NH2-MIL-125 (Ti) heterostructure with enhanced photodegradation efficiency for organic pollutants through synergistic effect. *Mater. Sci. Semicond. Process.* **97**, 91–100 (2019).
15. Ding, Y.-H. *et al.* A visible-light driven Bi_2S_3@ ZIF-8 core–shell heterostructure and synergistic photocatalysis mechanism. *Dalton Trans.* **47**(3), 684–692 (2018).
16. Zhang, X. *et al.* Synthesis of In_2S_3/UiO-66 hybrid with enhanced photocatalytic activity towards methyl orange and tetracycline hydrochloride degradation under visible-light irradiation. *Mater. Sci. Semicond. Process.* **91**, 212–221 (2019).
17. Wang, H. *et al.* Bi_2S_3@ NH_2-UiO-66-S composites modulated by covalent interfacial reactions boost photodegradation and the oxidative coupling of primary amines. *New J. Chem.* **45**(26), 11831–11844 (2021).
18. Farrag, M. Ultrasmall bimetallic Ru-Co alloy nanoclusters immobilized in amino-functionalized UiO-66 and N-doped carbonaceous zirconium oxide nanocomposite for hydrogen generation. *J. Alloy. Compd.* **920**, 165893 (2022).
19. Farrag, M. Comparative study of size-selected gold clusters (Au_{38}) and gold nanoparticles over porous cerium-based metal–organic frameworks with UiO-66 architecture for aerobic oxidation of cinnamyl alcohol. *Res. Chem. Intermed.* **47**, 2589–2604 (2021).
20. Cavka, J. H. *et al.* A new zirconium inorganic building brick forming metal organic frameworks with exceptional stability. *J. Am. Chem. Soc.* **130**, 13850 (2008).
21. Schaate, A. *et al.* Modulated synthesis of Zr-based metal–organic frameworks: From nano to single crystals. *Chem. Eur. J.* **17**, 6643 (2011).
22. Wang, M. *et al.* Heterostructured Bi_2S_3@ NH_2-MIL-125(Ti) nanocomposite as a bifunctional photocatalyst for Cr(VI) reduction and rhodamine B degradation under visible light. *RSC Adv.* **8**(22), 12459–12470 (2018).
23. Paul, K. K. *et al.* Solar light driven photoelectrocatalytic hydrogen evolution and dye degradation by metal-free few-layer MoS_2 nanoflower/TiO_2 (B) nanobelts heterostructure. *Sol. Energy Mater. Sol. Cells* **185**, 364–374 (2018).
24. Zhang, W., Wang, L. & Zhang, J. Preparation of Ag/UiO-66-NH_2 and its application in photocatalytic reduction of Cr (VI) under visible light. *Res. Chem. Intermed.* **45**, 4801–4811 (2019).
25. Swain, G. *et al.* A review on vertical and lateral heterostructures of semiconducting 2D-MoS2 with other 2D materials: A feasible perspective for energy conversion. *Nanoscale* **13**, 9908 (2021).
26. Alama, U. *et al.* Direct Z-scheme-based novel cobalt nickel tungstate/graphitic carbon nitride composite: Enhanced photocatalytic degradation of organic pollutants and oxidation of benzyl alcohol. *Colloids Surf. A* **630**, 127606 (2021).
27. Tripathy, S. P. *et al.* Metal organic framework-based Janus nanomaterials: Rational design, strategic fabrication and emerging applications. *Dalton Trans.* **51**, 5352 (2022).
28. Subudhi, S. *et al.* Metal oxide integrated metal organic frameworks (MO@MOF): Rational design, fabrication strategy, characterization and emerging photocatalytic applications. *Inorg. Chem. Front.* **8**, 1619 (2021).
29. Behera, P. *et al.* MOF derived nano-materials: A recent progress in strategic fabrication, characterization and mechanistic insight towards divergent photocatalytic applications. *Coord. Chem. Rev.* **456**(1), 214392 (2022).
30. Tripathy, S. P. *et al.* Inter-MOF hybrid (IMOFH): A concise analysis on emerging core–shell based hierarchical and multifunctional nanoporous materials. *Coord. Chem. Rev.* **434**(1), 213786 (2021).
31. Panda, J. *et al.* Inner transition metal-modulated metal organic frameworks (IT-MOFs) and their derived nanomaterials: A strategic approach towards stupendous photocatalysis. *Nanoscale* **15**(17), 7640 (2023).
32. Alam, U. *et al.* Photocatalytic oxidation of glyphosate and reduction of Cr(VI) in water over ACF-supported $CoNiWO_4$-gCN composite under batch and flow conditions. *Chemosphere* **297**, 134119 (2022).
33. Alam, U. *et al.* An anthraquinone-integrated S-scheme-based $NiTiO_3$-g-C_3N_4 composite with enhanced hydrogen production activity. *Int. J. Hydrog. Energy* **48**(7), 2532 (2023).
34. Farrag, M., Tschurl, M. & Heiz, U. Chiral gold and silver nanoclusters: Preparation, size selection, and chiroptical properties. *Chem. Mater.* **25**(6), 862–870 (2013).
35. Farrag, M. Microwave-assisted synthesis of ultra small bare gold clusters supported over Al_2O_3 and TiO_2 as catalysts in reduction of 4-nitrophenol to 4-aminophenol. *Microporous Mesoporous Mater.* **232**, 248–255 (2016).

36. Farrag, M. *et al.* Infra-red spectroscopy of size selected Au_{25}, Au_{38} and Au_{144} ligand protected gold clusters. *Phys. Chem. Chem. Phys.* **15**(30), 12539–12542 (2013).
37. Farrag, M. *et al.* Preparation and spectroscopic properties of monolayer-protected silver nanoclusters. *J. Phys. Chem. C* **116**(14), 8034–8043 (2012).
38. Farrag, M. Enantioselective silver nanoclusters: Preparation, characterization and photoluminescence spectroscopy. *Mater. Chem. Phys.* **180**, 349–356 (2016).
39. Farrag, M. Monodisperse and polydisperse platinum nanoclusters supported over TiO_2 anatase as catalysts for catalytic oxidation of styrene. *J. Mol. Catal. A* **413**, 67–76 (2016).
40. Farrag, M. *et al.* Ligand protected ultrasmall Pd nanoclusters supported on metal oxide surfaces for CO oxidation: Does the ligand activate or passivate the Pd nanocatalyst?. *ChemPhysChem* **22**(3), 312–322 (2021).
41. Farrag, M. Preparation of mesoporous palladium nanoclusters supported over hematite (α-Fe_2O_3) for selective catalytic hydrogenation of α, β-unsaturated aldehydes. *Microporous Mesoporous Mater.* **257**, 110–117 (2018).
42. Katz, M. J. *et al.* A facile synthesis of UiO-66, UiO-67 and their derivatives. *Chem. Commun.* **49**(82), 9449–9451 (2013).
43. Ge, Z.-H. *et al.* Low-cost, abundant binary sulfides as promising thermoelectric materials. *Mater. Today* **19**(4), 227–239 (2016).
44. Li, H. *et al.* MoS_2 Quantum dots decorated NH_2-MIL-125 heterojunction: Preparation and visible light photocatalytic performance. *J. Inorg. Mater.* **34**, 205 (2019).
45. AbdulHalim, L. G. *et al.* A scalable synthesis of highly stable and water dispersible $Ag_{44}(SR)_{30}$ nanoclusters. *J. Mater. Chem. A* **1**(35), 10148–10154 (2013).
46. Mohamed, O. S. *et al.* Nanoparticles TiO_2-photocatalyzed oxidation of selected cyclohexyl alcohols. *J. Photochem. Photobiol. A* **200**(2–3), 209–215 (2008).
47. Mohamed, O. S. *et al.* TiO_2 Nanoparticles-photocatalytic oxidation of selected cycloalkanols. *Int. J. Photoenergy* **2008**, 1–11 (2008).
48. Abdel-Wahab, A. M. A. *et al.* Ag-doped TiO_2 enhanced photocatalytic oxidation of 1,2-cyclohexanediol. *J. Phys. Org. Chem.* **25**(12), 1418–1421 (2012).
49. Guan, Z.-C. *et al.* Enhanced photoelectrochemical performances of ZnS-Bi_2S_3/TiO_2/WO_3 composite film for photocathodic protection. *Corros. Sci.* **143**, 31–38 (2018).
50. Lalithambika, K., Shanmugapriya, K. & Sriram, S. Photocatalytic activity of MoS_2 nanoparticles: An experimental and DFT analysis. *Appl. Phys. A* **125**, 1–8 (2019).
51. Rouquerol, J. *Characterization of Porous Solids* (Elsevier, 1994).
52. Jiang, X. *et al.* Facile synthesis of MoS_2/reduced graphene oxide composites for efficient removal of Cr (VI) from aqueous solutions. *RSC Adv.* **7**(39), 24149–24156 (2017).
53. Su, Y. *et al.* $Cd_{0.2}Zn_{0.8}S$@UiO-66-NH_2 nanocomposites as efficient and stable visible-light-driven photocatalyst for H2 evolution and CO_2 reduction. *Appl. Catal. B* **200**, 448 (2017).
54. Wang, X. *et al.* Visible light Bi_2S_3/$BiFeO_3$ photocatalyst for effective removal of Rhodamine B. *MATEC Web Conf.* **238**, 03007 (2018).
55. Ahmadpour, N. *et al.* A hierarchical Ca/TiO_2/NH_2-MIL-125 nanocomposite photocatalyst for solar visible light induced photodegradation of organic dye pollutants in water. *RSC Adv.* **10**, 29808 (2020).
56. He, L. *et al.* A novel amorphous CoS_x/NH_2-MIL-125 composite for photocatalytic degradation of rhodamine B under visible light. *J. Mater. Sci.* **55**, 16171 (2020).
57. Zhu, S.-R. *et al.* Enhanced photocatalytic performance of BiOBr/NH_2-MIL-125(Ti) composite for dye degradation under visible light. *Dalton Trans.* **45**, 17521 (2016).
58. Sabarinathan, M. *et al.* Highly efficient visible-light photocatalytic activity of MoS_2-TiO_2 mixtures hybrid photocatalyst and functional properties. *RSC Adv.* **7**, 24754 (2017).
59. Gao, L. *et al.* Cysteine-assisted synthesis of CuS-TiO_2 composites with enhanced photocatalytic activity. *Ceram. Int.* **43**, 9559 (2017).
60. Yang, X. *et al.* Preparation of CdS/TiO_2 nanotube arrays and the enhanced photocatalytic property. *Ceram. Int.* **42**, 7192 (2016).
61. Ullah, K. *et al.* Synthesis and characterization of novel PbS-graphene/TiO_2 composite with enhanced photocatalytic activity. *J. Ind. Eng. Chem.* **20**, 1035 (2014).

Acknowledgements

This work was financially supported by Assiut University, Egypt.

Author contributions

M. F. wrote the main manuscript text and prepared figures 1-9. The author reviewed the manuscript".

Funding

Open access funding provided by The Science, Technology & Innovation Funding Authority (STDF) in cooperation with The Egyptian Knowledge Bank (EKB).

Competing interests

The author declares no competing interests.

Additional information

Supplementary Information The online version contains supplementary material available at https://doi.org/10.1038/s41598-023-44819-8.

Correspondence and requests for materials should be addressed to M.F.

Reprints and permissions information is available at www.nature.com/reprints.

Publisher's note Springer Nature remains neutral with regard to jurisdictional claims in published maps and institutional affiliations.